ChemComm

COMMUNICATION

View Article Online
View Journal | View Issue

Cite this: *Chem. Commun.*, 2025, **61**, 13405

Received 17th March 2025,
Accepted 30th July 2025

DOI: 10.1039/d5cc01504a

rsc.li/chemcomm

Glass transition-induced luminescence in ZIF-62

Shuaihua Yu,[ab] Haitao Hu,[b] Yichao Lin, *[b] Wen Yang*[a] and Ziqi Tian *[bc]

We reported that ZIF-62 glass exhibits enhanced luminescence upon glass transition, contrasting with the crystalline phase fluorescence quenching caused by ordered ligand arrangement. Theoretical simulations combining *ab initio* molecular dynamics and quantum mechanical calculations reveal specific configurations in the glassy state with intensified emission, which are corroborated by experiments.

Metal–organic frameworks (MOFs) have garnered considerable attention owing to their versatile structures and potential applications in catalysis, gas storage, and optoelectronics.[1–5] Among MOFs, zeolitic imidazolate frameworks (ZIFs) are distinguished by their thermal stability and structural diversity. Notably, aside from their well-established crystalline forms, certain ZIFs can be produced in a glassy state *via* melt-quenching processes.[6–9] ZIF glasses represent a novel class of materials characterized by hybrid chemistry arising from the integration of inorganic and organic components. In these materials, metal nodes and organic ligands are connected *via* coordination bonds to form a zeolitic tetrahedral network, in which silicon or aluminum atoms are replaced by transition metal cations and oxygen is substituted by organic ligands.[10] For example, ZIF-62 is a prototypical porous framework that can be transformed into a glass. In ZIF-62, Zn^{2+} or Co^{2+} serves as the node, while imidazole (IM) and benzimidazole (BIM) function as the organic ligands.[11,12] ZIF-62 exhibits a low melting temperature and a broad melting range, undergoing melting prior to decomposition without recrystallization.[13]

Despite significant advances in the study of ZIF glasses, investigations into their optical properties remain relatively limited.[14–19] Qiao *et al.* first reported the optical properties of ZIF-62 glass, demonstrating a high transmittance (up to 90%) in both the visible and near-infrared regions, with a refractive index comparable to that of inorganic glasses.[20] Subsequently, Ali *et al.* observed mid-infrared luminescence in ZIF-62 glass containing both Zn and Co cations, attributing the emission to the d–d transition of the Co cation. The fluorescence intensity is enhanced with increasing Co concentration.[10] Furthermore, Liu *et al.* observed a more pronounced fluorescence difference between amorphous ZIF-62 glass obtained *via* the melt-quenching method and that synthesized by simple thermal methods below the melting temperature. This difference is supposed to be attributed to the structural variations between these two forms.[21] We note that the luminescence of the ZIF-62 crystal has rarely been reported. In the crystalline state, parallel stacking of adjacent BIM ligands may lead to aggregation-induced quenching. However, since BIM derivatives are commonly employed as fluorescent probes,[22,23] we hypothesize that the ligand in ZIF-62, which undergoes a specific rearrangement during the glass transition, may induce enhanced fluorescence.

Here, we synthesized ZIF-62 glass following the process shown in Fig. 1a.[24] The X-ray diffraction (XRD) pattern of the as-synthesized ZIF-62 crystal (Fig. 1c) confirmed a high degree of crystallinity, with all observed peaks matching those reported for ZIF-62.[12,24] In contrast, after the melt-quenching process, the disappearance of Bragg diffraction peaks signified a variation from the crystalline arrangement, thereby confirming the successful transformation of ZIF-62 into an amorphous phase. Thermogravimetric analysis (TGA) revealed a total weight loss of approximately 3.8% for the ZIF-62 powder up to 340 °C (Fig. S2). Specifically, around 0.7% mass loss occurred below 200 °C, corresponding to the release of water adsorbed within the ZIF-62 nanopores. An additional 3.1% mass loss was observed between 200 and 340 °C due to the incomplete removal of the DMF solvent during synthesis and purification. Further heating to 500 °C resulted in negligible mass change, confirming the high thermal stability of the ZIF-62 powder. Fourier-transform infrared (FTIR) spectra of the ZIF-62 crystal powder and ZIF-62 glass films are nearly identical, although

[a] *School of Materials Science and Engineering, Taiyuan University of Science and Technology, Taiyuan, Shanxi 030024, China. E-mail: yangwen@tyust.edu.cn*
[b] *Ningbo Institute of Materials Technology and Engineering, Chinese Academy of Sciences, Ningbo, Zhejiang 315201, China. E-mail: yclin@nimte.ac.cn, tianziqi@nimte.ac.cn*
[c] *University of Chinese Academy of Sciences, Yuquan Rd, Shijingshan District, Beijing 100049, China*

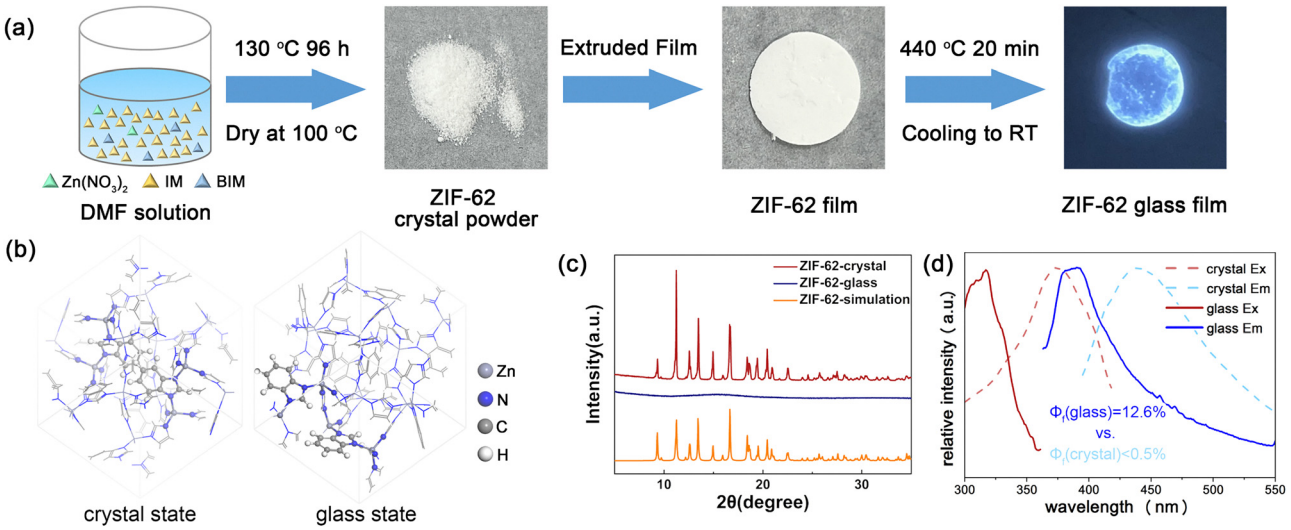

Fig. 1 (a) Experimental preparation process of ZIF-62 glass. (b) Crystalline and glassy structures. The closely packed and disordered ligands are highlighted using the ball-and-stick model. (c) XRD patterns. (d) Absorption (Ex) and emission (Em) spectra of the ZIF-62 crystal and glass samples.

additional peaks at 1679, 2857, 2931, and 3106 cm^{-1} (Fig. S3) are evident in the crystal powder spectrum. These peaks, associated with the DMF molecule, disappeared after the melt-quenching process, in agreement with the TGA–DSC characterization. Furthermore, the absorption and emission spectra were measured in both the crystalline and glassy states. In the crystalline state of our prepared sample, the absorption peak was located at 375 nm, with no apparent emission (quantum yield $< 0.5\%$). Upon transitioning to the glassy state, the absorption peak shifted to 320 nm, while a pronounced fluorescence emission at 390 nm was observed.

To understand the significantly enhanced emission of ZIF-62 in the glassy state, we performed *ab initio* molecular dynamics (AIMD) simulations to investigate variations in the packing patterns of the ligands during the glass transition. Previous studies have underscored the utility of AIMD in elucidating the microscopic structures of ZIF glasses. For instance, Gaillac *et al.* employed AIMD to demonstrate that both the chemical nature of the IM linker and the framework topology influence post-quenching behavior and the properties of the resulting glass.[25] Shi *et al.* utilized AIMD to analyze the melt structures of various ZIFs.[26] The computational studies reproduced the melt-quenching process, thereby advancing the understanding of the roles of topology and chemistry in governing the glass structure. In our simulations, we focused on the stacking arrangements of adjacent BIM units. The crystalline structure depicted in Fig. 2a served as the initial configuration.[27] The Vienna *ab initio* simulation package (VASP)[28] was used to optimize the pristine cell of ZIF-62 and to perform AIMD simulations within the canonical (NVT) ensemble. The PBE functional was employed with PAW for the density functional theory (DFT) calculation. For further methodological details, see the SI. To model the formation of ZIF-62 glass, the system was first heated to 800 K for 30 ps. The final snapshot was then optimized to emulate rapid cooling and to prevent recrystallization (Fig. 2b). Subsequently, a dynamics simulation was

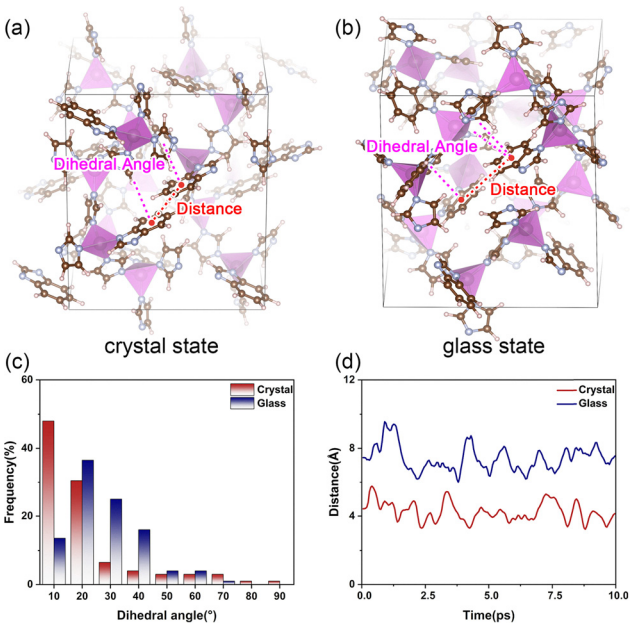

Fig. 2 (a) Representation of the ZIF-62 crystal. (b) Snapshot of the simulated ZIF-62 glass. (c) The distribution of the dihedral angles between adjacent BIM ligands in two states. (d) The evolutions of the average distances between the centers of the benzene rings in the neighboring BIM ligands in two states. The analyzed dihedral angle and distance are marked in the above figures.

conducted at 300 K for 10 ps from the relaxed structure to generate trajectories for topological analysis and following optical property simulations. For comparison, a dynamics simulation starting from the crystalline structure was performed at 300 K.

From Fig. 2c, one can see that the benzene rings of the BIM ligand in the crystalline state are aligned parallel and in close proximity. After the simulated melt-quenching process, the

ligands exhibit a disordered arrangement.[29] The Zn–Zn radial distribution function (RDF) presented in Fig. S4 illustrates that the crystalline framework has transformed into an amorphous state.[30] To quantify changes in the stacking of BIM ligands, 200 evenly spaced snapshots were extracted from each trajectory for the analysis of dihedral angles and distances of the neighboring BIM ligands. As shown in Fig. 2d, dihedral angle analysis reveals that adjacent BIM ligands in the ZIF-62 crystal remain nearly parallel at 300 K. Upon transitioning to the glassy state, the dihedral angle increases notably, with the dominant range shifting from approximately 0–20° to 10–40°. Additionally, the average distance between the centers of the neighboring benzene rings of BIM ligands increases apparently following the glass transition, suggesting that the departure of the conjugated groups may mitigate aggregation-induced quenching.

To explore the luminescence properties, six cluster models, each comprising two neighboring Zn nodes and four ligands connecting to each node, were constructed based on randomly selected configurations extracted from the dynamic trajectories of the glassy state. In comparison, one cluster model was built based on the pristine ZIF-62 crystal as well. The absorption and emission spectra, along with the fluorescence quantum yields, were simulated *via* quantum chemical calculations based on the cluster model.[31–33] Using the Gaussian16 package,[34] the geometries of both the ground state (S0) and the first excited state (S1) were optimized at the CAM-B3LYP/6-311G**/SDD level. Given the relative rigidity of the framework and the fact that the frontier orbitals are governed by the BIM ligands (Fig. S5), the positions of IM units were constrained during structural relaxation. Based on optimized structures, the absorption and emission spectra of the cluster models were simulated. The absorption wavelengths of various models range from 260 to 392 nm, corresponding to emission from 274 to 428 nm (see Table 1). As shown in Fig. 3a, most of the absorption peaks are within the experimental spectral range. Since all conformations contribute to the absorption, we consider the simulated absorption spectra to be reasonable. On the other hand, only specific configurations that exhibit high quantum yields correspond to intense fluorescence emission; herein the non-adiabatic transition process was considered *via* MOMAP,[35] which is designed for analyzing the photophysical properties of luminescent materials. The vibronic couplings and non-radiative decay processes can be simulated to more accurately estimate the fluorescence spectrum.

Table 1 The calculated absorption and emission properties of various cluster models derived from crystalline and glassy states

Model no.	Ex (nm)	Em (nm)	k_r (s^{-1})	k_{nr} (s^{-1})	Φ_f
1	392	407	6.94×10^5	1.43×10^7	4.64×10^{-2}
2	316	358	6.59×10^4	1.35×10^8	4.87×10^{-4}
3	287	292	6.21×10^5	3.13×10^9	1.98×10^{-4}
4	260	274	4.34×10^4	4.56×10^8	9.52×10^{-5}
5	308	323	1.37×10^5	1.62×10^9	8.45×10^{-5}
6	330	374	4.33×10^4	1.56×10^{11}	2.78×10^{-7}
Crystal	360	428	2.93×10^4	2.08×10^8	1.41×10^{-4}
Exp. crystal	375	440			$<5 \times 10^{-3}$
Exp. glass	320	390			1.26×10^{-1}

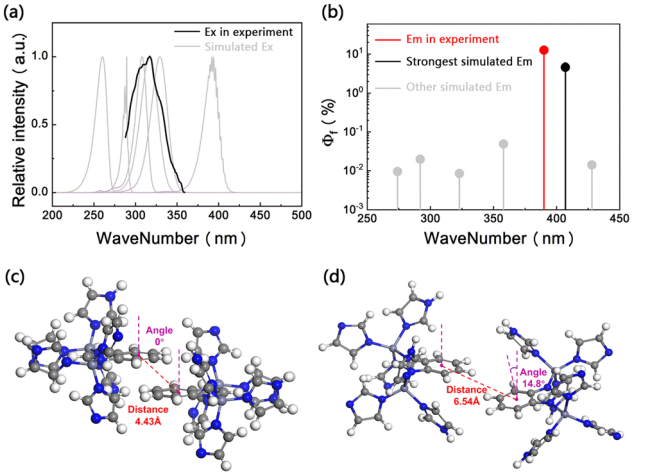

Fig. 3 (a) The simulated absorption spectrum based on the cluster models. (b) The emission wavelengths of the examined configurations of the glassy state. (c) The arrangement of BIM ligands in the crystalline state. (d) The arrangement of the BIM ligand in the configuration with the largest Φ_f.

Here, the radiative (k_r) and non-radiative (k_{nr}) decay rates were computed by using MOMAP. The fluorescence quantum yield (Φ_f), which represents the probability of deactivation *via* radiative decay, is determined by

$$\Phi_f = \frac{k_r}{k_r + k_{nr}}$$

For the cluster model derived from the crystalline structure, k_r and k_{nr} were 2.93×10^4 and 2.08×10^8 s^{-1}, respectively, yielding an extremely low Φ_f of 1.41×10^{-4}.[35] Thus, the fluorescence of the pristine ZIF-62 crystal should be quite weak. In contrast, among the six examined cluster models of the glassy state, three exhibited higher Φ_f values compared to the crystalline model. Notably, the model with the highest calculated Φ_f (0.0464, or 4.64%) displayed k_r and k_{nr} of 6.94×10^5 and 1.43×10^7 s^{-1}, respectively, with an emission wavelength of 407 nm. The Φ_f of the glass sample in the experiment was determined to be 12.6%, and thus the simulated absorption and emission spectra align well with the experimental measurements (Fig. 3b). The reasons of the discrepancy may include incomplete sampling of conformational space, the difference between the cluster model and the real periodic system, and inherent methodological errors. Nevertheless, specific configurations generated during the glass transition enhance fluorescence by 10^0–10^2 times relative to the crystalline state. In the configuration with the highest calculated Φ_f (Fig. 3c and d), the dihedral angle between adjacent BIM ligands is 14.80°, indicating that the two conjugated ligands remain nearly parallel. Concurrently, the distance between the centers of the benzene rings in the BIM ligands increases from 4.43 Å in the crystal to 6.54 Å in this configuration, suggesting that the glass transition process leads to an enlargement of certain micropores and a relative displacement of adjacent ligands. As a result, the fluorescence emission is significantly enhanced.

In summary, we propose that the close stacking of BIM ligands in the crystalline state leads to fluorescence quenching, whereas in the glassy state the disordered arrangement of BIM ligands weakens π–π interactions, thereby enhancing the fluorescence intensity. Our combined use of experimental characterization, AIMD simulations, and quantum chemical calculations supports this hypothesis and provides deeper insight into the glass transition-induced fluorescence in ZIF-62. The π–π stacking may lead to luminescence quenching in MOFs. The quenching mechanism arises from competing photophysical processes that dissipate excited-state energy non-radiatively. In the ZIF-62 crystal, π-conjugated BIM molecules stack closely, and thus their excited states can couple to emit with low quantum yields due to increased non-radiative decay pathway. Here, the glass transition results in the disordered arrangement of neighboring ligands, thus enhancing luminescence. In common MOFs, it may modulate the ligand arrangement and thus influence the luminescence by introducing large guest molecules. This ligand-disorder strategy is potentially applicable to other framework glasses; for instance, disrupting long-range order *via* melt-quenching or chemical modification can similarly mitigate aggregation-induced quenching by isolating emissive ligands or reducing exciton coupling. These findings not only advance our understanding of fluorescence in ZIF glasses but also pave the way for designing fluorescent materials with tailored properties towards various applications.

We thank Gao Yang from HZWTECH for helpful instructions. This work was financially supported by the Ministry of Industry and Information Technology of the People's Republic of China (Grant No. 2024ZD0607700), the National Natural Science Foundation of China (No. 52271232), the Ningbo Youth Science and Technology Leading Talents Project (2023QL026), and the Youth Innovation Promotion Association, CAS (No. 2020300).

Conflicts of interest

There are no conflicts to declare.

Data availability

All the data supporting this article have been included in the main text and the SI.

The method, experimental spectra and all the coordinates of the simulated species are included. See DOI: **https://doi.org/10.1039/d5cc01504a**

Notes and references

1 W. Fan, X. Zhang, Z. Kang, X. Liu and D. Sun, *Coord. Chem. Rev.*, 2021, **443**, 213968.
2 D. Liu, W. Gu, L. Zhou, L. Wang, J. Zhang, Y. Liu and J. Lei, *Chem. Eng. J.*, 2022, **427**, 131503.
3 D. Luo, C. Li, Y. Zhang, Q. Ma, C. Ma, Y. Nie, M. Li, X. Weng, R. Huang, Y. Zhao, L. Shui, X. Wang and Z. Chen, *Adv. Mater.*, 2022, **34**, e2105541.
4 B. Zhou, Z. Qi and D. Yan, *Angew. Chem., Int. Ed.*, 2022, **61**, e202208735.
5 Z. Yang, Y. Belmabkhout, L. N. McHugh, D. Ao, Y. Sun, S. Li, Z. Qiao, T. D. Bennett, M. D. Guiver and C. Zhong, *Nat. Mater.*, 2023, **22**, 888–894.
6 V. Nozari, O. Smirnova, J. M. Tuffnell, A. Knebel, T. D. Bennett and L. Wondraczek, *Adv. Mater. Technol.*, 2022, **7**, 2200343.
7 M. Kim, H. S. Lee, D. H. Seo, S. J. Cho, E. C. Jeon and H. R. Moon, *Nat. Commun.*, 2024, **15**, 1174.
8 D. Li, Z. Yang, L. Yang, C. Ma, M. Ye, Y. Sun, Z. Qiao and A. Chen, *J. Membr. Sci.*, 2024, **695**, 122492.
9 W. L. Xue, C. Das, J. B. Weiss and S. Henke, *Angew. Chem., Int. Ed.*, 2024, **63**, e202405307.
10 M. A. Ali, J. Ren, T. Zhao, X. Liu, Y. Hua, Y. Yue and J. Qiu, *ACS Omega*, 2019, **4**, 12081–12087.
11 K. Zhou, B. Mousavi, Z. Luo, S. Phatanasri, S. Chaemchuen and F. Verpoort, *J. Mater. Chem. A*, 2017, **5**, 952–957.
12 R. Lin, M. Chai, Y. Zhou, V. Chen, T. D. Bennett and J. Hou, *Chem. Soc. Rev.*, 2023, **52**, 4149–4172.
13 T. D. Bennett and A. K. Cheetham, *Acc. Chem. Res.*, 2014, **47**, 1555–1562.
14 R. Medishetty, J. K. Zareba, D. Mayer, M. Samoc and R. A. Fischer, *Chem. Soc. Rev.*, 2017, **46**, 4976–5004.
15 S. Horike, N. Ma, Z. Fan, S. Kosasang and M. M. Smedskjaer, *Nano Lett.*, 2021, **21**, 6382–6390.
16 J. K. Zaręba, M. Nyk and M. Samoć, *Adv. Opt. Mater.*, 2021, **9**, 2100216.
17 K. Fabrizio, K. N. Le, A. B. Andreeva, C. H. Hendon and C. K. Brozek, *ACS Mater. Lett.*, 2022, **4**, 457–463.
18 Y. Liang, W. Hu, X. Yuan, Z. Zeng, B. Zhu and Y. Gu, *Adv. Opt. Mater.*, 2022, **10**, 202200779.
19 S. Mehrzad Sajjadinezhad, L. Boivin, K. Bouarab and P. D. Harvey, *Coord. Chem. Rev.*, 2024, **510**, 215794.
20 A. Qiao, H. Tao, M. P. Carson, S. W. Aldrich, L. M. Thirion, T. D. Bennett, J. C. Mauro and Y. Yue, *Opt. Lett.*, 2019, **44**, 1623–1625.
21 S. Liu, Z. R. Wang, X. Lin, B. Y. Guo, S. Cai, W. G. Zhang, J. Fan and S. R. Zheng, *Inorg. Chem.*, 2024, **63**, 18574–18580.
22 E. Horak, P. Kassal and I. Murković Steinberg, *Supramol. Chem.*, 2017, **30**, 838–857.
23 Y.-C. Wu, J.-Y. You, K. Jiang, H.-Q. Wu, J.-F. Xiong and Z.-Y. Wang, *Dyes Pigm.*, 2018, **149**, 1–7.
24 Y. Wang, H. Jin, Q. Ma, K. Mo, H. Mao, A. Feldhoff, X. Cao, Y. Li, F. Pan and Z. Jiang, *Angew. Chem., Int. Ed.*, 2020, **59**, 4365–4369.
25 R. Gaillac, P. Pullumbi, T. D. Bennett and F.-X. Coudert, *Chem. Mater.*, 2020, **32**, 8004–8011.
26 Z. Shi, A. Arramel, T. D. Bennett, Y. Yue and N. Li, *iScience*, 2022, **25**, 104351.
27 J. Gandara-Loe, R. Bueno-Perez, A. Missyul, D. Fairen-Jimenez and J. Silvestre-Albero, *ACS Appl. Nano Mater.*, 2021, **4**, 3519–3528.
28 G. Kresse and J. Furthmüller, *Comput. Mater. Sci.*, 1996, **6**, 15–50.
29 T. Lu and F. Chen, *J. Comput. Chem.*, 2011, **33**, 580–592.
30 W. Humphrey, A. Dalke and K. Schulten, *J. Mol. Graphics*, 1996, **14**, 33–38.
31 K. Hendrickx, D. E. P. Vanpoucke, K. Leus, K. Lejaeghere, A. Van Yperen-De Deyne, V. Van Speybroeck, P. Van Der Voort and K. Hemelsoet, *Inorg. Chem.*, 2015, **54**, 10701–10710.
32 K. Hendrickx, J. J. Joos, A. De Vos, D. Poelman, P. F. Smet, V. Van Speybroeck, P. Van Der Voort and K. Lejaeghere, *Inorg. Chem.*, 2018, **57**, 5463–5474.
33 M. Ingham, A. Aziz, D. Di Tommaso and R. Crespo-Otero, *Mater. Adv.*, 2023, **4**, 5388–5419.
34 M. J. Frisch, *et al.*, *Gaussian 16, Revision C.03*, Gaussian, Inc., Wallingford CT, 2016. Full reference is provided in SI.
35 Z. Shuai, *Chin. J. Chem.*, 2020, **38**, 1223–1232.

